

Semi-Lagrangian lattice Boltzmann method for compressible flows

Dominik Wilde,^{1,2,*} Andreas Krämer,³ Dirk Reith,^{2,4} and Holger Foyssi¹

¹*Department of Mechanical Engineering, University of Siegen,
Paul-Bonatz-Straße 9-11, 57076 Siegen-Weidenau, Germany*

²*Institute of Technology, Resource and Energy-efficient Engineering (TREE),*

Bonn-Rhein-Sieg University of Applied Sciences, Grantham-Allee 20, 53757 Sankt Augustin, Germany

³*National Heart, Lung, and Blood Institute, National Institutes of Health, Bethesda, MD 20892, United States*

⁴*Fraunhofer Institute for Algorithms and Scientific Computing (SCAI),*

Schloss Birlinghoven, 53754 Sankt Augustin, Germany

(Dated: May 29, 2022)

This work introduces a semi-Lagrangian lattice Boltzmann (SLLBM) solver for compressible flows (with or without discontinuities). It makes use of a cell-wise representation of the simulation domain and utilizes interpolation polynomials up to fourth order to conduct the streaming step. The SLLBM solver allows for an independent time step size due to the absence of a time integrator and for the use of unusual velocity sets, like a D2Q25, which is constructed by the roots of the fifth-order Hermite polynomial. The properties of the proposed model are shown in diverse example simulations of a Sod shock tube, a two-dimensional Riemann problem and a shock-vortex interaction. It is shown that the cell-based interpolation and the use of Gauss-Lobatto-Chebyshev support points allow for spatially high-order solutions and minimize the mass loss caused by the interpolation. Transformed grids in the shock-vortex interaction show the general applicability to non-uniform grids.

I. INTRODUCTION

In the field of weakly compressible and isothermal flows, the lattice Boltzmann method (LBM) [1–3] has emerged as an efficient numerical solver that suits modern, highly-parallel computing architectures. Consequently, many attempts have been undertaken to extend the method to energy conserving flows [4]. Nonetheless, even 30 years after the LBM’s inception, a “genuine lattice Boltzmann model” [5] for compressible flows is still lacking.

Existing approaches can generally be categorized in two ways [6]: on- versus off-lattice, and single- versus double-population. While on-lattice approaches inherit the LBM’s exact, space-filling streaming step [5, 7, 8], off-lattice methods discretize the Boltzmann equation through finite volume [9, 10] or finite difference schemes [11–13]. Orthogonal to this classification, single-population models [4, 14] express all physical moments, including energy and heat flux, by a single distribution function. In order to represent all moments, the particle velocity sets have to be extended beyond the lattices typically used for weakly compressible flows. In contrast, double-population models [8, 15, 16] represent the local internal energy through a separate distribution function that is coupled with the density and momentum coming from the first distribution function.

The works of Frapolli [14] and Coreixas [17] present an excellent overview of compressible extensions of the LBM. They show how previous approaches have traditionally suffered from instability, numerical dissipation, large computational cost, and undesirable couplings between the physical and numerical parameters.

The present manuscript advances the methods available for compressible LBM simulations by combining two recent developments, a semi-Lagrangian streaming step [18] and a Hermite-based construction of higher-order velocity sets and equilibria [19]. We present a novel double-population off-lattice approach that mitigates the aforementioned issues of previous solvers and provides a more comprehensive solution for simulating compressible flows with the LBM.

The use of an efficient off-lattice method is key, since compressible on-lattice Boltzmann methods suffer from decisive disadvantages. First, the time step size is set to unity and cannot be changed independently from the physical parameters. In the weakly compressible regime, the Mach number is merely a numerical parameter following the law of similarity, so that the time step size can be changed via the flow velocity [6]. In compressible flows, however, the Mach number regains its meaning as a physical quantity with only limited remaining options to change the time step, e.g by increasing or decreasing the spatial resolution, which is still coupled to the time step size. Alternatively, the speed of sound can be varied, at the price of a inferior numerical stability [4]. Second, the simulation of energy conserving flows requires disproportionately large velocity sets since integer-based values of the particle velocities lead to leading-order errors in the relevant moments of the Maxwell-Boltzmann distribution function [20]. A common way to reduce these errors is to increase the number of abscissae, leading to velocity sets like D1Q7, D2Q49 or D3Q343 [21]. For weakly compressible flows, the D1Q3 velocity set and its tensor products D2Q9 and D3Q27 in combination with a second-order truncation of the Maxwell-Boltzmann distribution mostly match the desired properties of the Navier-Stokes equations in the hydrodynamic limit, except the “famous $O(Ma^3)$ error term” [22], which breaks Galilean invari-

* wilde.aerospace@gmail.com

ance and restricts simulations to low Mach numbers.

The physical and numerical parameters can be decoupled in an off-lattice framework, where the velocity set does not need to match the computational grid. In the field of off-lattice Boltzmann methods the semi-Lagrangian lattice Boltzmann method (SLLBM) was recently introduced [18] and further investigated in a number of subsequent works [23–27]. To formulate the streaming step the algorithm follows the trajectories of the lattice Boltzmann equation along their characteristics to find the cells of the corresponding departure points. In each cell, a finite element formulation reconstructs the distribution function values from the local degrees of freedom by interpolation polynomials. The SLLBM overcomes the aforementioned drawbacks of the standard lattice Boltzmann method. It decouples the time step from the grid spacing and allows for high-order spatial accuracy on irregular grids. In common with Eulerian-based off-lattice Boltzmann solvers the SLLBM enables the use of non-integer-based velocity sets. Yet, compared to Eulerian-based off-lattice Boltzmann schemes, the streaming step is computationally more efficient [26], reduces numerical dissipation, and is still close to the original formulation of the LBM, as it also follows the trajectories of the discrete Boltzmann equation back in time [18]. In a notable recent work Dorschner et al. also showed that the SLLBM can also be formulated in a local reference frame [25] which recovers Galilei invariance in the LBM, similar to other adaptive LBM models for compressible flows [28–30].

The semi-Lagrangian streaming step also offers more flexibility in constructing velocity sets from Hermite polynomials [19, 31], which is particularly relevant for compressible flow. Originating in Grad’s work on the moment system in kinetic theory [32], a number of subsequent works showed that consistent equilibrium distribution functions can be derived by projecting the Boltzmann equation onto a low-dimensional Hilbert subspace through Hermite expansion [19, 20, 33]. This method is used to construct high-order velocity sets that recover the compressible Fourier-Navier-Stokes equations in the hydrodynamic limit [22, 34].

This article is structured as follows. Section II derives the equilibria and velocity sets and recapitulates the semi-Lagrangian advection scheme. Section III validates the method by simulations of a Sod shock tube, a two-dimensional Riemann problem, and a shock-vortex interaction. Section IV discusses the properties of the compressible SLLBM and highlights the advantages over other compressible LBM solvers. Section V provides conclusions.

II. METHODOLOGY

The Boltzmann equation reads

$$\partial_t f + \xi \cdot \nabla f = \Omega(f) \quad (1)$$

with the particle distribution f , the particle velocities ξ and the collision operator Ω . In this work, only the linearized single relaxation time collision operator proposed by Bhatnagar-Gross-Krook (BGK) [35] will be used:

$$\Omega(f) = -\frac{1}{\lambda} (f - f^{\text{eq}}), \quad (2)$$

where f^{eq} denotes the equilibrium distribution function, while the relaxation time $\lambda = \nu/c_s^2$ reflects the kinematic viscosity ν and the speed of sound c_s .

The macroscopic density (ρ), velocity (u), and energy (E) are represented by the moments of the distribution function:

$$\rho = \int f d\xi \quad (3)$$

$$\rho u = \int f \xi d\xi \quad (4)$$

$$2\rho E = \int (f \xi^2 + g) d\xi, \quad (5)$$

The second distribution function g represents the rotational energy of the polyatomic molecules and is described in subsection II C.

A. Equilibrium distribution function

One key component to correctly calculate thermal and compressible flows is the construction of the equilibrium distribution function f^{eq} . The equilibrium is found via scaled Hermite polynomials $H^{(n)}(\hat{\xi})$, which are formulated in terms of the normalized particle velocities $\hat{\xi} = \xi/c_s$. The Hermite polynomials are defined by the generating function

$$\omega(\hat{\xi}) = \frac{1}{\sqrt{2\pi}} \exp\left(-\frac{\hat{\xi}^2}{2}\right) \quad (6)$$

as

$$\mathcal{H}^{(n)}(\hat{\xi}) = (-1)^n \frac{1}{\omega(\hat{\xi})} \frac{d^n}{d\hat{\xi}^n} \omega(\hat{\xi}), \quad (7)$$

where $c_s^2 = RT_0$ is the product of gas constant and reference temperature. (Note that the generating function is differentiated with respect to ξ rather than $\hat{\xi}$.)

The scaled Hermite polynomials in one dimension up to fourth order are

$$\begin{aligned} \mathcal{H}^{(0)} &= 1 \\ \mathcal{H}^{(1)} &= \frac{\hat{\xi}}{c_s} \\ \mathcal{H}^{(2)} &= \frac{\hat{\xi}^2 - 1}{c_s^2} \\ \mathcal{H}^{(3)} &= \frac{\hat{\xi}^3 - 3\hat{\xi}}{c_s^3} \\ \mathcal{H}^{(4)} &= \frac{\hat{\xi}^4 - 6\hat{\xi}^2 + 3}{c_s^4} \end{aligned}$$

The Hermite coefficients \mathbf{a} are directly related to the mo-

ments of the Maxwell-Boltzmann equilibrium.

$$a^{(0)} = \rho \quad (8a)$$

$$a_{\alpha}^{(1)} = \rho u_{\alpha} \quad (8b)$$

$$a_{\alpha\beta}^{(2)} = \Pi_{\alpha\beta} = \rho(u_{\alpha}u_{\beta} + T_0(\theta - 1)\delta_{\alpha\beta}) \quad (8c)$$

$$a_{\alpha\beta\gamma}^{(3)} = \mathcal{Q}_{\alpha\beta\gamma} = \rho[u_{\alpha}u_{\beta}u_{\gamma} + T_0(\theta - 1)(\delta_{\alpha\beta}u_{\gamma} + \delta_{\alpha\gamma}u_{\beta} + \delta_{\beta\gamma}u_{\alpha})] \quad (8d)$$

$$a_{\alpha\beta\gamma\delta}^{(4)} = \mathcal{R}_{\alpha\beta\gamma\delta} = \rho[u_{\alpha}u_{\beta}u_{\gamma}u_{\delta} + T_0(\theta - 1)((T_0(\theta - 1)(\delta_{\alpha\beta}\delta_{\gamma\delta} + \delta_{\alpha\gamma}\delta_{\beta\delta} + \delta_{\alpha\delta}\delta_{\beta\gamma}) + \delta_{\alpha\beta}u_{\gamma}u_{\delta} + \delta_{\alpha\gamma}u_{\beta}u_{\delta} + \delta_{\alpha\delta}u_{\beta}u_{\gamma} + \delta_{\beta\gamma}u_{\alpha}u_{\delta} + \delta_{\beta\delta}u_{\alpha}u_{\gamma} + \delta_{\gamma\delta}u_{\alpha}u_{\beta})] \quad (8e)$$

Note that in case of the established weakly compressible lattice Boltzmann simulations, the isothermal assumption leads to a local temperature of $\theta = T/T_0 = 1$ and to vanishing terms in Eqs. (8).

Finally, the equilibrium distribution function can be expressed as a Hermite series

$$f^{\text{eq},N}(\hat{\xi}) \approx \omega(\hat{\xi}) \sum_{n=0}^N \frac{1}{n!} a^{(n)}(\mathbf{x}, t) \cdot \mathcal{H}^{(n)}(\hat{\xi}). \quad (9)$$

The order N determines the physics of the lattice Boltzmann model. Truncating at second order covers the well-known lattice Boltzmann model for weakly compressible flows at low velocity. Truncating at third order compromises the non-equilibrium parts of $\mathcal{Q}_{\alpha\beta\gamma}$ due to deviations in $\mathcal{R}_{\alpha\beta\gamma\delta}^{\text{eq}}$. Thus, to represent the heat flux correctly, a fourth-order expansion is required [22, 33]. Consequently, to recover the full Fourier-Navier-Stokes equations, the sum in equation (9) is of fourth order in the present work.

B. Hermite polynomial velocity sets

To recover the M th order moment a^M , the velocity space is discretized by a (weighted) Gauss-Hermite quadrature

$$a^M = \int f^{\text{eq},N} \mathcal{H}^M d\hat{\xi} = \sum_{i=1}^V f_i^{\text{eq},N} \mathcal{H}^M(\hat{\xi}_i), \quad (10)$$

provided $N \geq M$ and with the discrete equilibrium

$$f_i^{\text{eq},N} = w_i/w(\hat{\xi}_i) \cdot f^{\text{eq},N}(\hat{\xi}_i).$$

Here, w_i represents the weights coming from a Gauss-Hermite quadrature, V is the number of velocities in the velocity set. In general, the number of possible velocity sets is several times larger than in on-lattice Boltzmann methods, since the abscissae of the velocity sets are not required to match the grid points. The present work uses a D2Q25 velocity set, which is derived by a tensor

TABLE I. Abscissae ξ_i and weights w_i for the D1Q5 lattice. The D2Q25 velocity set is obtained by a tensor multiplication.

i	ξ_i	w_i
0	0	8/15
1, 3	$\pm\sqrt{5 - \sqrt{10}}$	$7 + 2\sqrt{10}/60$
2, 4	$\pm\sqrt{5 + \sqrt{10}}$	$7 - 2\sqrt{10}/60$

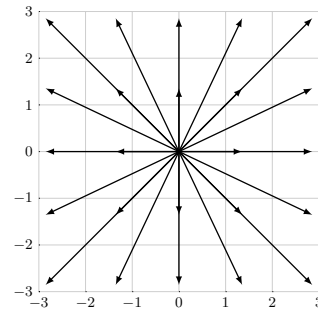


FIG. 1. D2Q25 velocity set based on Hermite polynomials of order 5. Although the velocity can be scaled, matching the regular grid is not possible.

multiplication from the one-dimensional D1Q5 velocity set [19]. The one-dimensional abscissae and weights are listed in Table I, while the two-dimensional D2Q25 velocity set is depicted in Fig. 1. Unless scaled, the characteristic lattice speed of sound equals $c_s = 1$.

This off-lattice velocity set is of quadrature order $Q = 9$ and consequently recovers moments up to order $N = 4$, fulfilling the requirement $(M + N)/2 \leq Q$ to recover the Fourier-Navier-Stokes equations [19].

C. Variable heat capacity ratio

In the context of thermal and compressible flows, the usage of the BGK operator limits the Prandtl number Pr , i.e. the ratio of kinematic viscosity ν and thermal

diffusivity α , to $Pr = \nu/\alpha = 1$. This drawback can be circumvented by using a multi-relaxation time collision operator to decouple both properties of the fluid [36], a quasi-equilibrium [5, 37] or by using a BGK-Shakhov model [38]. Concerning the Euler test cases of the Sod shock tube and the 2D Riemann problem in Section III this has no consequences, but in case of the shock-vortex interaction this possibly leads to minimal deviations in the acoustic plots. In addition, as the Boltzmann equation and the Maxwell-Boltzmann distribution are valid in the assumption of monoatomic flows, the heat capacity ratio $\gamma = C_p/C_v$ is fixed to $\gamma = (D + 2)/2$, with the dimension D and the heat capacities at constant pressure and volume C_p and C_v , respectively. Nonetheless, several attempts in the literature solve this issue by using a

second set of distribution functions [14, 39], inspired by the Rykov model in kinetic theory for polyatomic gases [40], or by adapting the equilibrium distribution to the heat capacity of the fluid [41]. We adopt the ansatz by Frapolli et al. for the LBM by incorporating an additional set of distributions g and its equilibrium g^{eq} .

The equilibrium of g^{eq} can easily be determined as

$$g_i^{\text{eq}} = (2C_v - D)T f_i^{\text{eq}} \quad (11)$$

with $\gamma = R/C_v + 1$, where the gas constant R is usually set to unity (without loss of generality). The distribution function g_i follows the same stream and collide algorithm as the distribution function f_i .

The lattice Boltzmann equations of the present model read

$$f_i(x, t) = f_i(x - \delta_t \xi_i, t - \delta_t) - \frac{1}{\tau} [f_i(x - \delta_t \xi_i, t - \delta_t) - f_i^{\text{eq}}(x - \delta_t \xi_i, t - \delta_t)] \quad (12a)$$

$$g_i(x, t) = g_i(x - \delta_t \xi_i, t - \delta_t) - \frac{1}{\tau} [g_i(x - \delta_t \xi_i, t - \delta_t) - g_i^{\text{eq}}(x - \delta_t \xi_i, t - \delta_t)], \quad (12b)$$

with the relaxation time $\tau = \nu/(c_s^2 \delta_t) + 0.5$, where the term of 0.5 is a consequence of the second-order time integration in terms of the trapezoidal rule [42–44]. In contrast to the usual lattice Boltzmann algorithm, neither the time step size δ_t , nor the expression $\delta_t \xi_i$ are required to be integers due to the use of a semi-Lagrangian streaming step.

D. Semi-Lagrangian streaming step

Instead of a point-wise representation of the distribution function values f_i (and likewise g_i), the SLLBM uses a cell-wise polynomial interpolation. Therefore, the computational domain is divided into a finite number of cells N_{Ξ} with Lagrange polynomials ψ_{Ξ} of order p as shape functions. The distribution function values at the support points in cell Ξ are denoted as $\hat{f}_{i\Xi j}$, so that

$$f_i(\mathbf{x}, t) = \sum_{\Xi=1}^{N_{\Xi}} \sum_{j=1}^{N_j} \hat{f}_{i\Xi j}(t) \psi_{\Xi j}(\mathbf{x}) \quad (13)$$

for all points \mathbf{x} in cell Ξ .

The distributions $\hat{f}_{i\Xi j}$ are updated via the Equations (12), where the value at the departure point $f_i(x - \delta_t \xi_i)$ is obtained via the interpolation defined in Eq. (13). An equidistant interpolation is stable for low order interpolation polynomials only. Therefore, at higher interpolation orders this work applies Gauß-Lobatto-Chebyshev support points to dampen the Runge phenomenon and to increase the stability. [18, 45]. Gauß-Lobatto-Chebyshev support points in one dimension read

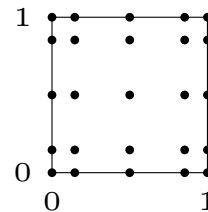


FIG. 2. Distribution of Gauß-Lobatto-Chebyshev support points on a two-dimensional reference cell with $p = 4$.

$$x_k = \frac{1}{2} \left[-\cos \left(\frac{k-1}{n-1} \pi \right) + 1 \right], \quad k = 1, 2, \dots, n.$$

The two-dimensional unit cell used in this work is depicted in Fig. 2.

E. Thermo-hydrodynamic limit

The thermo-hydrodynamic limit of the presented equilibrium distribution function was presented and thoroughly discussed by Malaspinas et al. [34] and by Coreixas et al. [22], who found

$$\partial_t(\rho) + \partial_\alpha(\rho u_\alpha) = 0 \quad (14)$$

$$\begin{aligned} \partial_t(\rho u_\alpha) + \partial_\beta(\rho u_\alpha u_\beta) &= \partial_\alpha \sigma_{\alpha\beta} \\ \partial_t(\rho E) + \partial_\alpha(\rho E u_\alpha) &= \partial_\alpha(\kappa \partial_\alpha T) + \partial_\alpha(\sigma_{\alpha\beta} u_\beta) \end{aligned} \quad (15)$$

with the stress tensor

$$\sigma_{\alpha\beta} = -p\delta_{\alpha\beta} + \nu\partial_\beta[\rho(\partial_\beta u_\alpha + \partial_\alpha u_\beta)] - \zeta\partial_\gamma u_\gamma\delta_{\alpha\beta}, \quad (16)$$

and with the heat conductivity $\kappa = \nu C_p/\rho$. The kinematic viscosity is defined as

$$\nu = \left(\tau - \frac{1}{2}\right)c_s^2\delta_t, \quad (17)$$

while the bulk viscosity equals

$$\zeta = \rho\nu\left(\frac{1}{C_v} - \frac{2}{D}\right), \quad (18)$$

depending on the heat capacity at constant volume C_v [21].

F. Minmod interpolation limiter

In common with many other numerical schemes for Euler or compressible Navier-Stokes equations, discontinuities in density or temperature lead to Gibbs oscillations near the shocks, which is the primary source for instabilities [46]. To cope with these numerical artifacts, the present work introduces a minmod interpolation limiter which maintains the interpolated value within the range of distribution function values in each cell. This procedure resembles minmod functions and flux limiters in Eulerian schemes at low additional computational effort [46] and is defined as follows

$$f_i(\mathbf{x}) = \begin{cases} \mathcal{P}_{i\Xi}(\mathbf{x}), & \text{if } \min_j \hat{f}_{i\Xi j} \leq \mathcal{P}_{i\Xi}(\mathbf{x}) \leq \max_j \hat{f}_{i\Xi j}, \\ \min_j \hat{f}_{i\Xi j}, & \text{if } \mathcal{P}_{i\Xi}(\mathbf{x}) < \min_j \hat{f}_{i\Xi j}, \\ \max_j \hat{f}_{i\Xi j}, & \text{if } \mathcal{P}_{i\Xi}(\mathbf{x}) > \max_j \hat{f}_{i\Xi j}, \end{cases}$$

with $\mathcal{P}_{i\Xi}(\mathbf{x}) = \sum_{j=1}^{N_j} \psi_{\Xi j}(\mathbf{x}) \hat{f}_{i\Xi j}$. The limiter will be applied in the Sod shock tube test case in Section III A.

III. RESULTS

In this section, three compressible test cases will be studied. First the Sod shock tube shows the general capability of the SLLBM to deal with shocks at the original density ratio presented by Sod [47]. Then the two-dimensional Riemann problem will be studied, followed a simulation of a shock-vortex interaction on non-uniform grids.

A. Sod shock tube

In a first test case, the well-known Sod shock tube [47] was simulated. The one-dimensional domain $x \in [0, 1]$ was divided into two regions at $x = 0.5$ with the initial conditions

TABLE II. Initial conditions of the 2D Riemann problem according to Lax and Liu [48].

$\rho = 1$	$\rho = 0.5313$
$u_x = 0.7276$	$u_x = 0$
$u_y = 0$	$u_y = 0$
$P = 1$	$P = 0.4$
$\rho = 0.8$	$\rho = 1$
$u_x = 0$	$u_x = 0$
$u_y = 0$	$u_y = 0.7276$
$P = 1$	$P = 1$

$$\begin{aligned} \rho_0 &= 8, u_0 = 0, P_0 = 10, \\ \rho_1 &= 1, u_1 = 0, P_1 = 1, \end{aligned}$$

with $P = \rho RT$ being the pressure according to the ideal gas law and $R = 1$. The periodic domain was discretized using 200 grid points. Consequently, the number of cells was 100 for $p = 2$ and 50 for $p = 4$. The kinematic viscosity and adiabatic exponent were set to $\nu = 0.00172$ and $\gamma = 1.4$, respectively. All results for this test case were simulated using the minmod interpolation limiter. With a time step size of $\delta_t = 0.00333$ this results in a relaxation time of $\tau = \nu/(c_s^2\delta_t) + 0.5 = 0.517$. Fig. 3 depicts the density, velocity, and temperature for the polynomial order $p = 2$ at $t = 0.15$, which is reached after 375 time steps. Fig. 4 depicts the results for $p = 4$.

For both polynomial orders, the results accurately matched the reference solution [47]. The high-order solution provoked minor oscillations in the smooth regions of the temperature field, but the minmod interpolation limiter still kept the solution close to the reference, even at this low resolution.

To compare both orders in detail, Fig. 5 depicts the slopes at a discontinuity. As expected, the spatially high-order solution allows for steeper slopes. Taken together, the Sod shock tube shows that the proposed SLLBM solver is capable to accurately capture shocks at a relatively low resolution.

B. 2D Riemann

The two-dimensional Riemann problem is another demanding test case for compressible inviscid flow solvers, which was deeply investigated for a variety of initial configurations by Lax and Liu [48] and Kurganov and Tadmore [49]. The original works made use of Riemann solvers and semi-discrete finite difference schemes, respectively, to obtain the reference solutions.

The domain $(x, y) \in [0, 1]$ was divided into four quadrants with the initial conditions shown in Table II. The simulation domain was discretized into $N_\Xi = 128 \times 128$ cells with an order of finite elements of $p = 4$, which

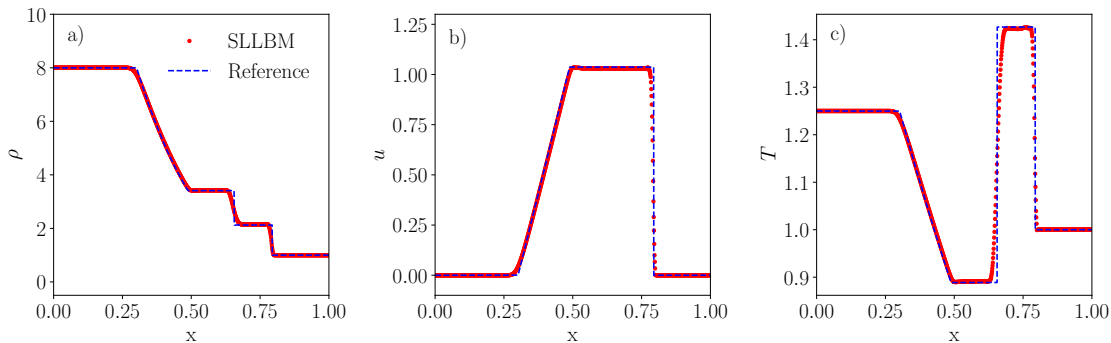


FIG. 3. Sod shock tube with $p = 2, N = 200, \delta t = 0.00333$ after 375 iterations showing a) density ρ , b) velocity u and c) temperature T . The SLLBM is compared with Sod's reference results [47].

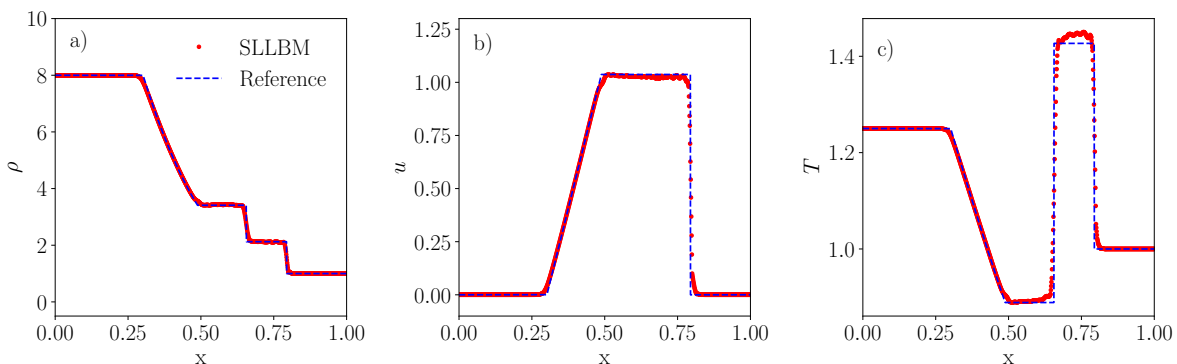


FIG. 4. Sod shock tube with $p = 4, N = 200, \delta t = 0.00333$ after 375 iterations showing a) density ρ , b) velocity u and c) temperature T . The SLLBM is compared with Sod's reference results [47].

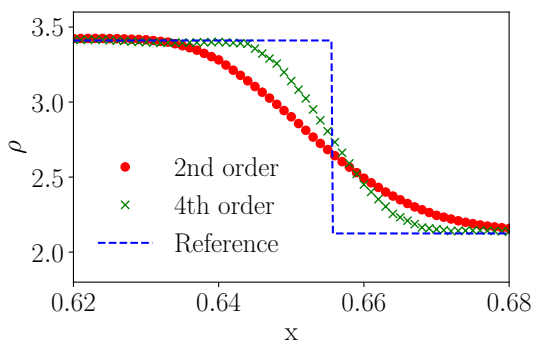


FIG. 5. Comparison of the slopes of the density in the Sod shock tube simulation with orders $p = 2$ and $p = 4$. The high-order polynomials allow for a steeper slope.

results in $N = 512 \times 512$ grid points. The relaxation time $\tau = 1.94815$ was determined according to $\tau = \nu / (c_s^2 \delta t) + 0.5$. The physical simulation end time was $t_{\text{end}} = 0.25$, which is reached after 2091 iterations, i.e. the viscosity is $\nu = 0.000173$, assuming the reference

temperature $T_0 = 1$. The heat capacity ratio was set to $\gamma = 1.4$. At the boundaries, a zero-gradient condition, i.e. $\partial f = 0$, was applied. From a practical point-of-view, to free the simulation domain from disturbing boundary interactions, the domain was set to twice the size and clipped during post-processing. At first, Gauss-Lobatto-Chebyshev nodes were used to distribute the support points within each cell. Fig. 6 shows the density contours after 2091 iterations. In total, 45 equally distributed contours were applied. The results were in good agreement with the reference solution in [48, 49], although minor oscillations were still visible near the shock fronts.

Fig. 7 depicts the pressure, velocity and temperature charts along the $y = x$ diagonal at the simulation end time. Although there is no reference solution available, the plot gives a good impression of the strong discontinuities that are also the main source of instabilities in this test case.

To emphasize the value of non-equidistant support points for the interpolation procedure, the same configuration was simulated again with equidistant nodes. The simulation became unstable shortly after 200 time steps. Fig. 8 shows the pressure along the $y = x$ axis and reveals

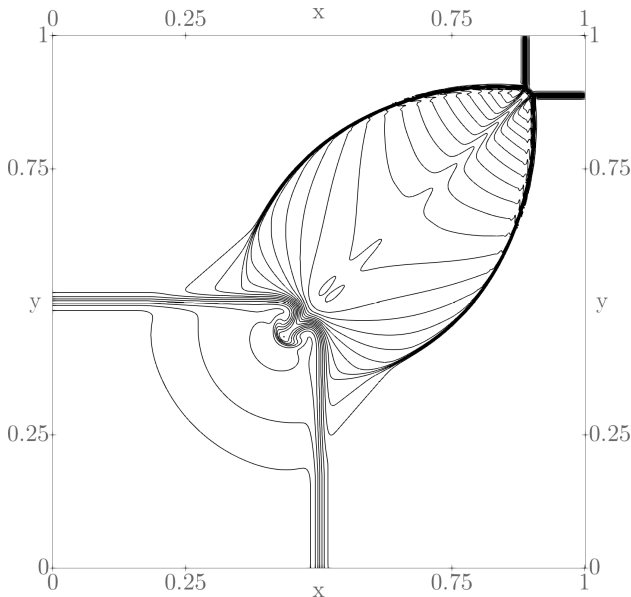


FIG. 6. Outline of 45 equally spaced density contours of the 2D Riemann problem with $N = 512 \times 512$ in the interval $\rho \in [0.412, 1.753]$. The order of finite elements was $p = 4$. The simulation end time was reached in 2091 iterations. Reference solutions obtained by two different solvers are available in [48] and [49]

the heavy oscillations of the simulation with equidistant nodes shortly before the simulation diverges.

C. Shock vortex interaction

The final test case was a 2D shock vortex interaction, which was originally presented by Inoue and Hattori [50]. For this simulation a transformed grid was used, which shows the applicability of the SLLBM to non-uniform grids. The simulation set-up was as follows: the domain consists of two regions, which are separated by a steady shock. The Mach number of region A is $Ma_A = -1.2$, while the Mach number in region B $Ma_B \approx -0.842$ is determined by the Rankine-Hugoniot condition. A vortex with characteristic Mach number $Ma_v = 0.5$ is advected in region A towards the shock (from right to left) and interacts with it throughout the simulation. The flow field of the vortex is given by:

$$u_\theta(r) = \sqrt{\gamma T} Ma_v r \exp((1 - r^2)/2) \quad (19)$$

The initial pressure and density field are

$$P(r) = \frac{1}{\gamma} \left(1 - \frac{\gamma - 1}{2} Ma_v \exp(1 - r^2) \right)^{\gamma/(\gamma-1)} \quad (20)$$

and

$$\rho(r) = \left(1 - \frac{\gamma - 1}{2} Ma_v \exp(1 - r^2) \right)^{1/(\gamma-1)}. \quad (21)$$

The temperature field can be determined via the ideal gas law $P = \rho RT$.

The Reynolds number is defined by

$$Re = 400 = \frac{c_s R}{\nu} \quad (22)$$

with R being the resolution of the characteristic radius r .

The simulation was run on a physical domain of size 72×24 , which was discretized by $N_\Xi = 128 \times 128$ cells and the polynomial order was $p = 4$, resulting in 512 lattice nodes in each direction. However, to highly resolve the steady shock the grid was transformed in x-direction according to a simple transformation function:

$$x_{\text{trans}} = \frac{36}{\pi} \left(\Lambda \sin \left(\frac{\pi}{36} (x + 6) \right) + \frac{\pi}{36} x \right), \quad (23)$$

where Λ is a stretching parameter, which was set to $\Lambda = 0.8$ in the first simulation. The shock was located at $x_{\text{shock}} = 30$ and the initial vortex center position was $x_{\text{vortex}} = 32$. The schematic grid is shown in Fig. 9. The average resolution of the characteristic radius along the x-axis r was $512/72 \approx 7.1$ grid points and $512/24 \approx 21.3$ grid points along the y-axis. The large domain and periodic boundary conditions in all directions were sufficient to keep the domain of interest free from disturbing influences of the boundaries. The simulation ran stable without using a minmod interpolation limiter, which was therefore not used. The characteristic time is defined as $t' = R/c_s$. The time step size was $\delta_t = 0.00686$ so that the final result at $t = 8$ was reached in 1165 iterations.

Fig. 10 shows the density contours in the range $\rho \in [0.78, 1.55]$ with 119 contours. The contours were in good agreement with previous works, e.g. [14, 50].

Since the SLLBM is not rigorously mass-conserving, we show the evolution of mass over 1500 simulation steps in Fig. 11. In case of a low-order polynomial interpolation of $p = 2$, there was a minor but steady loss of mass, which amounted to approximately 0.05% of the initial mass after 1500 steps. The mass conservation was tighter for the high-order interpolation. For $p = 4$, the mass oscillated around the initial value as opposed to a systematic gain or loss.

To quantify the results, the radial sound pressure in a simulation with $Ma_v = 0.25$ and $Re = 800$ was evaluated and compared with DNS results from Inoue and Hattori [50]. To ensure a high resolution of the shock-vortex interaction zone, the stretching factor was set to $\Lambda = 0.9$ and the time step size in this configuration was $\delta_t = 0.00390$. Fig. 12 shows the normalized pressure $\Delta P = (P - P_B)/P_B$, where P_B denotes the initial pressure in region B. All three plots slightly overestimate the width of the precursor, which might be due to the lower resolution far from the shock and to some extent due to the fixed Prandtl number of $Pr = 1$ in this work, while Inoue and Hattori used a Prandtl number of $Pr = 0.75$. Nonetheless, the chart shows a close match of the SLLBM with previous work.

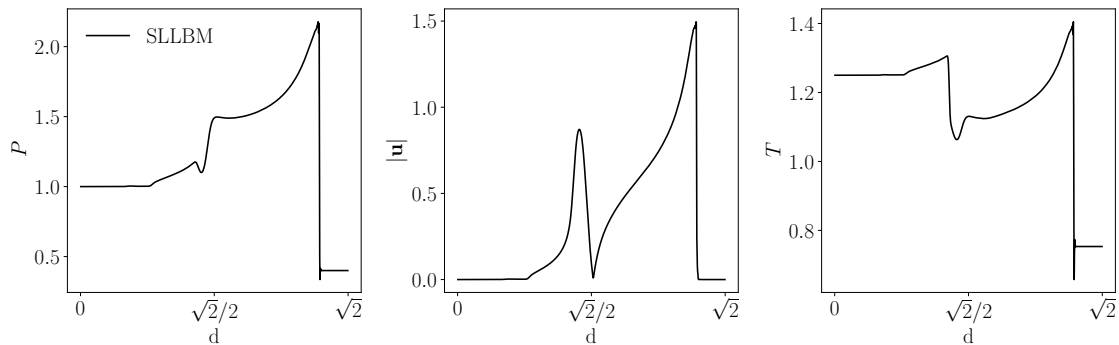


FIG. 7. Pressure, velocity and temperature curves of the two-dimensional Riemann problem, shown in Fig. 6 along the $y = x$ diagonal d .

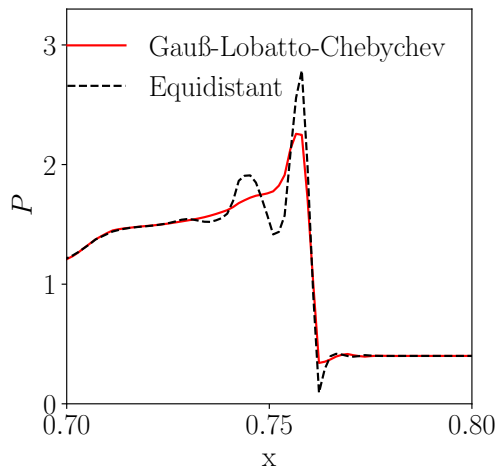


FIG. 8. Comparison of the pressure P with Gauß-Lobatto-Chebyshev nodes and conventional equidistant nodes at order of finite elements of $p = 4$ after 200 time steps. The test run with equidistant nodes provoked heavy oscillations, which resulted in a crash shortly afterwards.

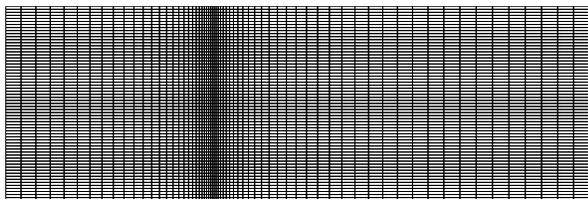


FIG. 9. Schematic grid for the shock vortex interaction. The actual grid used in the simulation was further refined by splitting each cell in half along each axis. Each cell contains 5×5 support points.

IV. DISCUSSION

As detailed in the introduction of this work, a best practice of lattice Boltzmann methods for compressible

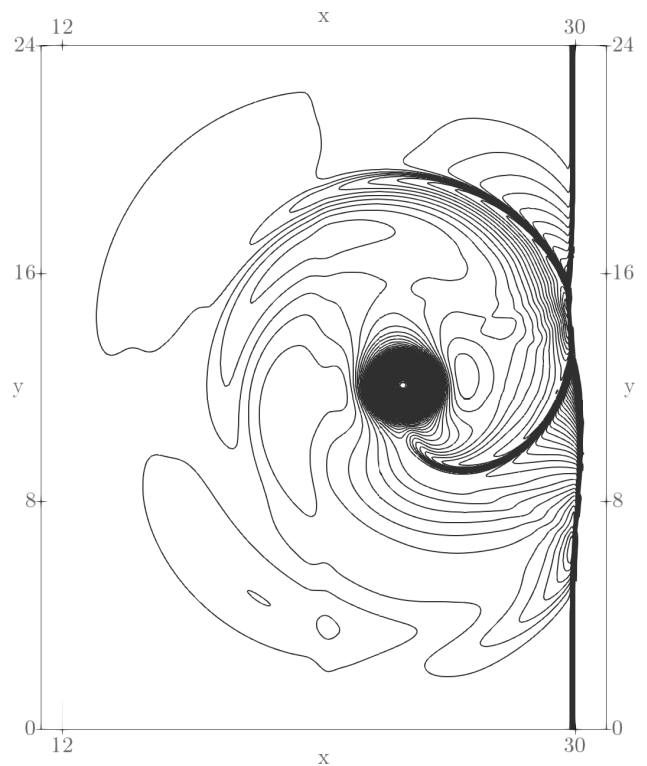


FIG. 10. Density contours of the shock-vortex interaction with $Ma_v = 0.5$ and $Re = 400$ in the range $\rho \in [0.78, 1.55]$ in 119 steps.

flows is missing. We have shown how the use of an efficient off-lattice streaming step enables compressible simulations by relaxing the coupling between time step, computational grid, and particle velocities in the LBM. Originating from the usual lattice Boltzmann equation the SLLBM algorithm follows the trajectories along the characteristics and recovers the off-lattice departure points using a cell-based finite element interpolation. In common with finite volume or finite difference LBMs, this procedure allows for a flexible time step size. This key

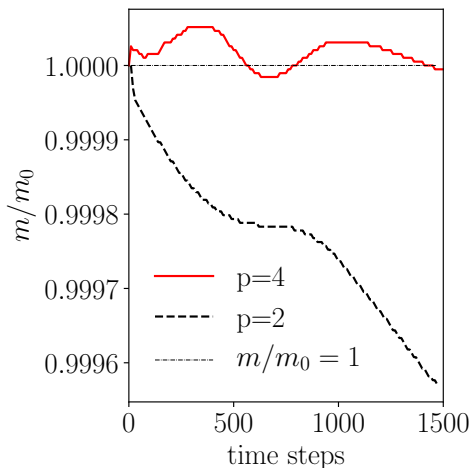


FIG. 11. Relative mass m/m_0 for polynomial orders $p = 4$ and $p = 2$ over the number of iterations for the test case shown in Fig. 10.

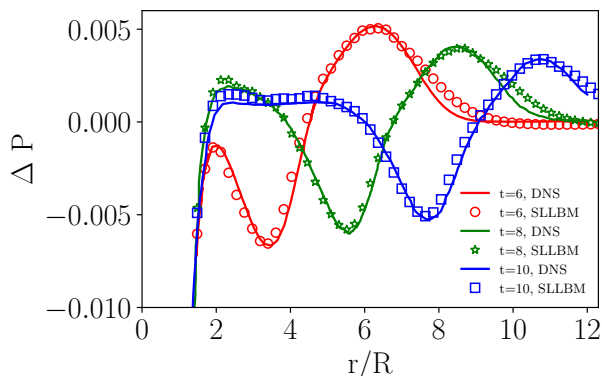


FIG. 12. Sound pressure $\Delta P = (P - P_B)/P_B$ of the shock-vortex interaction with $Re = 800$, $Ma_v = 0.25$ and $Ma_A = 1.2$ at times $t' = 6$, $t' = 8$, and $t' = 10$. The measurements were taken from the center of the vortex along the radius with -45° with respect to the x-axis. DNS from [50].

feature is missing in usual on-lattice Boltzmann solvers for compressible flows. Contrary to the Eulerian methods, the SLLBM avoids costly and often high-dissipative time integration.

We tested the compressible SLLBM for three common test cases, in both inviscid and viscous regimes. The Sod shock tube in its original configuration and a pressure ratio of $P_1/P_2 = 10$ was successfully tested with the SLLBM. In contrast, on-lattice Boltzmann solvers like the one presented in [8] often restrict the pressure ratio to lower values on larger grids, while a recursive regularization allowed to assure stability in the work by Coreixas et al. [22]. In contrast, the SLLBM's variable time step size allows to adapt the time step to the needs of the simula-

tion, even with the most common BGK model. Furthermore, we employed second and fourth order interpolation polynomials, rendering the solution in the smooth areas spatially to the corresponding order [18], which is another unique property of this scheme. However, as shown in the two-dimensional Riemann problem in section III B, leveraging the spatial order is only workable for an appropriate distribution of support points within each cell. While equidistant support points led to unstable simulations, the use of fourth order Gauss-Lobatto-Chebyshev points enabled stable simulations. Moreover, the simulation of the shock-vortex interaction showed that a high-order interpolation improves mass conservation, which is not rigorously enforced interpolation-based LBM [27]. Still, in common with other advection schemes, applying a high-order reconstruction often leads to spurious oscillations at the shock fronts. We presented a minmod interpolation limiter, which was successfully used to suppress spurious oscillations at the shock fronts of the Sod shock tube. Future works should therefore focus on the reduction of oscillations at the shock fronts to maintain the high order in smooth areas at high Reynolds numbers. The equilibrium distribution function based on a Hermite expansion of fourth order is computationally intense, but allows to represent compressible and viscous flows with energy conservation [33]. Concerning the discretization of the velocity space, a D2Q25 velocity set based on the fifth-order Hermite polynomial has been used, which is suited to recover the moments up to fourth order correctly [20]. In contrast, on-lattice velocity sets usually provoke deviations in the recovery of the high-order moments [20]. The combination of the equilibrium and velocity set allowed for a total Mach number of $Ma = 1.7$ in the simulation of the shock-vortex interaction.

Future works should thoroughly investigate the path to extend the velocity sets to higher velocities in three dimensions, while keeping the number of discrete velocities lower than 125. The effects of lattice pruning, which were thoroughly studied in the weakly compressible case, e.g. D3Q27 to D3Q19 [51], should also be examined for these high-order velocity sets. Besides this, the extensions of co-moving reference frames accompanied by high-order polynomial orders should also be evaluated [25]. Another issue is the second distribution function value, needed to correctly represent the heat capacity ratio γ . This model was also successfully used by other authors [5, 8, 14]. A reduction of the velocity set size of g could possibly make the compressible LBM more attractive.

All in all, the presented SLLBM solver for compressible flows convinces by six main advantages:

1. the flexibility of the time step size,
2. the absence of a costly time integrator,
3. the applicability to stretched or unstructured meshes
4. the possibility to employ advantageous velocity sets

5. the limitation of the mass loss by high-order polynomials, and
6. the simple, but efficient minmod interpolation limiter.

Taken together, the presented SLLBM at the same time opens a new field of solvers for compressible flows and combines many insights from previous LBM solvers for compressible flows.

V. CONCLUSIONS

In this article we showed that the semi-Lagrangian streaming step enables efficient lattice Boltzmann simulations of compressible flows. It is based on a cell-wise representation of the computational domain by utilizing interpolation polynomials up to fourth order. The method features a variable time step size, the absence

of a time integrator, a variable heat capacity ratio, and is able to incorporate non-integer based velocity sets. The test cases of a Sod shock tube, a 2D Riemann problem and a shock-vortex interaction on transformed grids show the general applicability to flows with discontinuities. Thereby, both the introduced interpolation limiter and the Gauss-Lobatto-Chebyshev support points allow to reduce oscillations near the shock fronts.

In our future work, the presented framework will be applied to three-dimensional test cases with a focus on reducing spurious oscillations and further increasing the time step size.

ACKNOWLEDGMENTS

This work was supported by the German Ministry of Education and Research and the Ministry for Culture and Science North Rhine-Westphalia (research grant 13FH156IN6). The authors would like to thank Ilya V. Karlin for fruitful discussions.

-
- [1] G. R. McNamara and G. Zanetti, Phys. Rev. Lett. (1988), 10.1103/PhysRevLett.61.2332.
 - [2] F. J. Higuera and J. Jiménez, EPL (1989), 10.1209/0295-5075/9/7/009.
 - [3] S. Chen, H. Chen, D. Martinez, and W. Matthaeus, Phys. Rev. Lett. (1991), 10.1103/PhysRevLett.67.3776.
 - [4] F. J. Alexander, H. Chen, S. Chen, and G. D. Doolen, Physical Review A **46**, 1967 (1992).
 - [5] N. Frapolli, S. S. Chikatamarla, and I. V. Karlin, Phys. Rev. E **92** (2015), 10.1103/PhysRevE.92.061301.
 - [6] T. Krüger, H. Kusumaatmaja, A. Kuzmin, O. Shardt, G. Silva, and E. M. Viggen, *The lattice Boltzmann method: Principles and practice* (2017).
 - [7] M. Atif, M. Namburi, and S. Ansumali, Phys. Rev. E **98**, 053311 (2018).
 - [8] M. H. Saadat, F. Bösch, and I. V. Karlin, Phys. Rev. E **99**, 013306 (2019).
 - [9] Z. Guo, R. Wang, and K. Xu, Phys. Rev. E **91**, 033313 (2015).
 - [10] Y. Feng, P. Sagaut, and W. Q. Tao, Computers and Fluids **131**, 45 (2016).
 - [11] W. Shi, W. Shyy, and R. Mei, Numerical Heat Transfer, Part B: Fundamentals **40**, 1 (2001).
 - [12] Y. Wang, Y. L. He, T. S. Zhao, G. H. Tang, and W. Q. Tao, International Journal of Modern Physics C **18**, 1961 (2007).
 - [13] X. Nie, X. Shan, and H. Chen, 47th AIAA Aerospace Sciences Meeting including The New Horizons Forum and Aerospace Exposition (2009), 10.2514/6.2009-139.
 - [14] N. Frapolli, *Entropic lattice Boltzmann models for thermal and compressible flows*, Ph.D. thesis (2017).
 - [15] T. Kataoka and M. Tsutahara, Phys. Rev. E (2004), 10.1103/PhysRevE.69.056702.
 - [16] Q. Li, Y. L. He, Y. Wang, and W. Q. Tao, Phys. Rev. E (2007), 10.1103/PhysRevE.76.056705.
 - [17] C. Coreixas, *High-order extension of the recursive regularized lattice Boltzmann method*, Ph.D. thesis (2018).
 - [18] A. Krämer, K. Küllmer, D. Reith, W. Joppich, and H. Foysi, Phys. Rev. E **95** (2017), 10.1103/PhysRevE.95.023305.
 - [19] X. Shan, Journal of Computational Science **17**, 475 (2016).
 - [20] S. S. Chikatamarla and I. V. Karlin, Phys. Rev. E **79** (2009), 10.1103/PhysRevE.79.046701.
 - [21] N. Frapolli, S. S. Chikatamarla, and I. V. Karlin, Phys. Rev. E **93**, 063302 (2016).
 - [22] C. Coreixas, G. Wissocq, G. Puigt, J. F. Boussuge, and P. Sagaut, Phys. Rev. E (2017), 10.1103/PhysRevE.96.033306, arXiv:1704.04413.
 - [23] A. Krämer, *Lattice-Boltzmann-Methoden zur Simulation inkompressibler Wirbelströmungen*, Ph.D. thesis (2017).
 - [24] G. Di Ilio, D. Chiappini, S. Ubertini, G. Bella, and S. Succi, Computers and Fluids (2018), 10.1016/j.compfluid.2018.02.014.
 - [25] B. Dorschner, F. Bösch, and I. V. Karlin, Phys. Rev. Lett. **121**, 130602 (2018).
 - [26] A. Krämer, D. Wilde, K. Küllmer, D. Reith, H. Foysi, and W. Joppich, *Comput. Math. with Appl.*, (2018), 10.1053/seiz.2001.0662.
 - [27] A. V. Zakirov, B. A. Korneev, V. D. Levchenko, and A. Y. Perepelkina, Keldysh Inst. Prepr. , 1 (2019).
 - [28] C. Sun, Phys. Rev. E - Stat. Physics, Plasmas, Fluids, Relat. Interdiscip. Top. **58**, 7283 (1998).
 - [29] C. Sun, J. Comput. Phys. **161**, 70 (2000).
 - [30] C. Sun and A. T. Hsu, Phys. Rev. E **68**, 14 (2003).
 - [31] A. Bardow, I. V. Karlin, and A. A. Gusev, Phys. Rev. E (2008), 10.1103/PhysRevE.77.025701.
 - [32] H. Grad, Communications on Pure and Applied Mathematics **2**, 331 (1949).
 - [33] X. Shan, X. F. Yuan, and H. Chen, Journal of Fluid Mechanics (2006), 10.1017/S0022112005008153.

- [34] O. Malaspinas, *Lattice Boltzmann Method for the Simulation of Viscoelastic Fluid Flows*, Ph.D. thesis (2009).
- [35] P. L. Bhatnagar, E. P. Gross, and M. Krook, *Physical Review* **94**, 511 (1954).
- [36] X. Shan and H. Chen, *International Journal of Modern Physics C* **18**, 635 (2007).
- [37] S. Ansumali, S. Arcidiacono, S. S. Chikatamarla, N. I. Prasianakis, A. N. Gorban, and I. V. Karlin, *The European Physical Journal B* **56**, 135 (2007).
- [38] E. M. Shakhov, *Fluid Dynamics* **3**, 95 (1972).
- [39] X. Nie, X. Shan, and H. Chen, *Phys. Rev. E* **77**, 1 (2008).
- [40] V. A. Rykov, *Fluid Dynamics* **10**, 959 (1976).
- [41] P. J. Dellar, *Progress in Computational Fluid Dynamics, An International Journal* (2008), 10.1504/PCFD.2008.018081.
- [42] X. He, X. Shan, and G. D. Doolen, *Phys. Rev. E - Stat. Physics, Plasmas, Fluids, Relat. Interdiscip. Top.* **57**, R13 (1998).
- [43] M. Krause, *Fluid Flow Simulation and Optimisation with Lattice Boltzmann Methods on High Performance Computers - Application to the Human Respiratory System*, Ph.D. thesis (2010).
- [44] D. Wilde, A. Krämer, K. Küllmer, H. Foyssi, and D. Reith, *Int. J. Numer. Methods Fluids* **90**, 156 (2019).
- [45] J. Hesthaven and T. Warburton, *J. Comput. Phys.* (2002), 10.1006/jcph.2002.7118.
- [46] J. S. Hesthaven and T. Warburton, *Texts Appl. Math.*, Vol. 54 (Springer, New York, 2008).
- [47] G. A. Sod, *Journal of Computational Physics* **27**, 1 (1978).
- [48] P. Lax and X. Liu, *SIAM Journal on Scientific Computing* **19**, 319 (1998).
- [49] A. Kurganov and E. Tadmor, *Numer. Methods Partial Differ. Equ.* (2002), 10.1002/num.10025.
- [50] O. Inoue and Y. Hattori, *J. Fluid Mech.* **380**, 81 (1999).
- [51] A. T. White and C. K. Chong, *J. Comput. Phys.* **230**, 6367 (2011).